Check for updates

Ultrafast Science
A SCIENCE PARTNER JOURNAL

RESEARCH ARTICLE

How Does a Ceramic Melt Under Laser? Tunnel Ionization Dominant Femtosecond Ultrafast Melting in Magnesium Oxide

Hui Zhao[1,2,3], Shiqi Hu[1,2], Mengxue Guan[1], Xinbao Liu[1,2], Daqiang Chen[1,2], Jiyu Xu[1,4*], and Sheng Meng[1,2,4*]

[1]Beijing National Laboratory for Condensed Matter Physics, Institute of Physics, Chinese Academy of Sciences, Beijing 100190, China. [2]School of Physical Sciences, University of Chinese Academy of Sciences, Beijing 100049, China. [3]Department of Complex Matter, Jozef Stefan Institute, Ljubljana 1000, Slovenia. [4]Songshan Lake Materials Laboratory, Dongguan, Guangdong 523808, China.

*Address correspondence to: jiyuxu@iphy.ac.cn (J.X.); smeng@iphy.ac.cn (S.M.)

Citation: Zhao H, Hu S, Guan M, Liu X, Chen D, Xu J, Meng S. How Does a Ceramic Melt Under Laser? Tunnel Ionization Dominant Femtosecond Ultrafast Melting in Magnesium Oxide. *Ultrafast Sci.* 2025;5:Article 0085. https://doi.org/10.34133/ultrafastscience.0085

Submitted 6 July 2024
Revised 19 October 2024
Accepted 14 December 2024
Published 5 February 2025

Copyright © 2025 Hui Zhao et al. Exclusive licensee Xi'an Institute of Optics and Precision Mechanics. No claim to original U.S. Government Works. Distributed under a Creative Commons Attribution License (CC BY 4.0).

Laser-induced melting plays a crucial role in advanced manufacturing technology and ultrafast science; however, its atomic processes and microscopic mechanisms, especially in a wide-gap ceramic, remain elusive due to complex interplays between many degrees of freedom within a timescale of ~100 fs. We report here that laser melting is greatly accelerated by intense laser-induced tunnel ionization, instead of a priori multiphoton absorption, in the archetypal ceramic magnesium oxide (MgO). The tunneling processes generate a large number of photocarriers and results in intense energy absorption, instantaneously altering the potential energy surface of lattice configuration. The strong electron–phonon couplings and fast carrier relaxation enable efficient energy transfer between electrons and the lattice. These results account well for the latest ultrafast melting experiments and provide atomistic details and nonequilibrium mechanism of photoinduced ultrafast phase transitions in wide-gap materials. The laser modulation of melting thresholds and phase boundary demonstrate the possibility of manipulating phase transition on demand. A shock wave curve is also obtained at moderate conditions ($P = 2$ GPa), extending Hugoniot curve to new regimes.

Introduction

In the past decades, the rapid advancements of ultrafast laser technologies have enabled the ultrafast nonequilibrium dynamics and controllable phase transitions in condensed matter [1,2]. The photoinduced electronic excitations not only manipulate the electronic properties of materials [3,4] but also instantaneously modulate lattice stabilities by changing the potential energy surfaces (PESs) of lattice configurations and ultrafast heating effects [5]. The photoinduced lattice instabilities and directional forces lead to ultrafast atomistic dynamics at subpicosecond timescales [6], e.g., ultrafast nonthermal melting or amorphization processes [7] and order-to-order structural transformations via specific phonon excitations [8–10]. For example, the strong electronic excitations of ~10% valence electrons to conduction bands featuring antibonding character were shown to trigger the ultrafast nonthermal melting in semiconductors, e.g., Si [11–13], Bi [14], Ge [2,15], and InSb [7]. On the other hand, the ultrafast heating effects originating from laser energy absorption and subsequent energy transfer also contribute to ultrafast thermal melting at a few picoseconds in metals [16–19], which may lead to macroscopic ablation phenomena [20]. Fortunately, by adequately optimizing operation setups, the laser-induced ultrafast melting can be employed to precisely process complex nanostructures of transparent material without macroscopic thermal damage [21,22].

Recently, the photoinduced ultrafast melting and subsequent welding was experimentally demonstrated in wide-gap hard ceramic materials with high melting temperatures [23], extending the melting objects from soft metals/semiconductors to hard insulating ceramics. However, the ultrafast mechanisms of photoionization, energy transfer, and atomistic dynamics of laser-induced ultrafast melting are lacking for these wide-gap crystalline materials. The linear single-photon absorption is the primary photoionization mechanism under weak laser irradiations for metals and semiconductors, while the nonlinear processes, e.g., multiphoton processes and tunnel ionizations, should also play a key role in photoionization under intense laser irradiations especially for wide-gap materials [20,22,24–26]. Furthermore, the coupled ionic motion and energy transfer pathway should resort to real-time nonadiabatic processes of photoexcited materials [12,13,27]. As an example, magnesium oxide (MgO) is one of the prototypical ceramic materials exhibiting a high melting temperature (~3,200 K) and a wide band gap (~6.0 eV). It is widely used in realistic applications owing to its excellent physical and chemical properties, and thus, the laser-induced ultrafast melting of MgO is critical to both manufacturing technologies and ultrafast science. In addition, the laser-induced extreme conditions provide a novel avenue to study extreme condition physics [28]. The experimental works studied the principal shock Hugoniot curve under high pressure (P) and temperature (T) conditions of MgO [28–31]. However,

Downloaded from https://spj.science.org at Institute of Physics, Cas on March 07, 2025

the reported minimum pressure of Hugoniot curve of MgO is ~100 GPa [29], and a precise and complete characterization on a wide range of *P*-*T* conditions is highly desirable.

In this work, we employ MgO as an example to investigate the nonequilibrium mechanisms of laser-driven ultrafast melting of wide-gap ceramic materials. Our study is based on real-time time-dependent density functional theory (rt-TDDFT) molecular dynamics (MD) simulations, which was shown to describe well the complex interplays among different degrees of freedom in photoexcited materials [6,10,12,26,32–34]. The intense 1,028-nm and 191-nm laser pulses with intensity I ranging from 0.76 to 47 TW/cm^2 are used to excite the MgO crystal. The detailed simulation methods are shown in Materials and Methods. We reveal that lattice melting is drastically enhanced under intense longer-wavelength laser pulse irradiations, which is attributed to strong-field-induced tunnel ionization. The tunnelling processes result in strong electronic excitations and energy absorptions. The changes of PES and heating of atomic systems both lead to the femtosecond lattice dynamics and melting processes of MgO. A shock wave curve can also be obtained at moderate pressure (P = 2 GPa), which extends Hugoniot curve to moderate conditions. The obtained melting line can be recognized as a unique boundary between B1 (NaCl-type structure) and liquid phases with nonequilibrium electronic states. Our work offers a first-step in-depth microscopic understanding of ultrafast homogeneous melting of ceramics in the ultimate timescale (~100 fs) and spatial scale (~1 nm) and presents an effective approach for rationally triggering ultrafast phase transitions using parameter-optimized laser pulses.

Methods

The TDDFT-MD simulations were carried out using the time-dependent ab initio package (TDAP) [35–38] based on SIESTA [39–41]. TDDFT-MD naturally includes nonadiabatic electron–electron scattering and electron–phonon scattering by solving time-dependent Kohn–Sham equations [42], and describes well the ultrafast nonadiabatic dynamics of MgO following photoexcitation. We employ the Troullier–Martin pseudopotentials [43] and the Perdew, Burke, and Ernzerhof (PBE) [44] exchange-correlation functional, and adopt the auxiliary real-space grid equivalent to a plane-wave cutoff of 300 Ry. The calculated band gap is ~2 eV, almost one-third of experimental gap of ~6.0 eV. The simulation cell contains 64 atoms of the NaCl-type (B1) phase of MgO [30]. The velocity gauge is used to enable the periodic electric fields in TDDFT-MD simulations. A Monkosrt–Pack grid of 3 × 3 × 3 is used to sample the Brillouin zone. The initial atomic position and velocity were sampled from a Born–Oppenheimer MD simulation at 300 K in constant particle number–volume–energy (NVE) ensembles. We use the time step of 0.05 fs for the electrons and ions in nonadiabatic simulations. The Gaussian wavepacket is used to represent the laser pulses, with the pulse width ~40 fs centered at t = ~50 fs. The laser intensity (I) ranges from 0.76 to 47 TW/cm^2. We choose the long-wavelength (LW) laser pulses of 1,028 nm (photon energy 1.2 eV, about half of the calculated band gap ~2 eV of MgO) to trigger the lattice dynamics of MgO crystal, which is similar to experimental setups [23]. At the same time, the short-wavelength (SW) laser pulses of 191 nm (photon energy 6.5 eV) are also employed to directly compare the linear and nonlinear photoexcitation and the succeeding lattice dynamics. We note that the photon energy 1.2 eV of long wavelength is less than both the calculated band gap of 2.0 eV and experimental band gap of 6.0 eV, and the photon energy 6.5 eV of short wavelength is greater than both the calculated band gap of 2.0 eV and experimental band gap of 6.0 eV. Therefore, the photoionization mechanisms are not changed despite the different band gaps.

Results

Figure 1 displays schematically the microscopic dynamics of MgO ultrafast melting process under intense laser irradiations. The lattice structure receives a large amount of heat energy under the irradiations of LW 1,028-nm laser pulses (photon energy ~1.2 eV, about half of the calculated band gap of 2 eV), while the heating effect is relatively weak under the SW 191-nm (photon energy ~6.5 eV) laser irradiation. What is more, the heating effects exhibit different tendencies with laser intensity for the 2 laser pulses. The obtained characteristic lattice structures are shown in the inset of Fig. 1A. It is clear that the LW laser pulses lead to severe structural distortions and amorphization, whereas the variations of the crystal structure are negligible under SW laser pulses. The distinct heat accumulations and lattice dynamics correspond to the diverse photoexcitation mechanisms and energy transfer pathways, which is dependent on the relationship between laser intensity, photon energy, and band gap of MgO. For the intense LW laser pulses used here, strong-field tunnel ionization gives rise to the substantial electronic excitations and energy absorptions (Fig. 1B), which also instantaneously changes the PES of lattice structures. However, due to the finite local electronic density of states in conduction band, the discrete single-photon and 2-photon excitation processes give the limited electronic excitation and energy absorptions by SW laser pulses (Fig. 1C).

The photoinduced lattice instabilities and melting processes can be determined with the Lindemann criterion [45,46]. According the Lindemann criterion, MgO crystal is considered to be melted when the atomic root mean square displacement

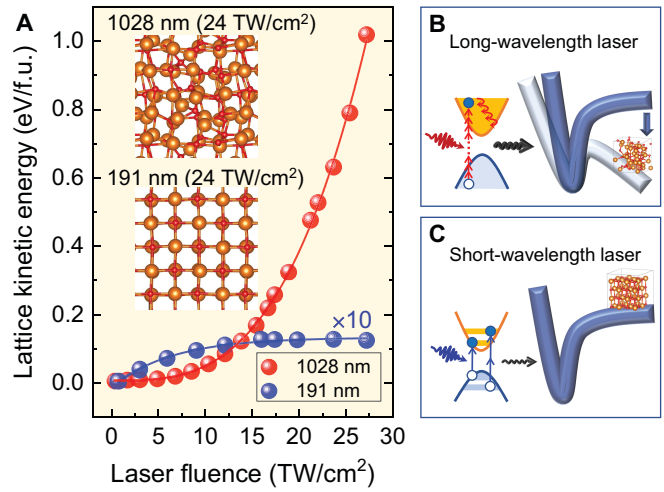

Fig. 1. The lattice heating effects with laser intensity and the microscopic mechanisms of laser melting. (A) Lattice kinetic energy at 100 fs as a function of laser intensity for SW 191-nm laser pulses and LW 1,028-nm laser pulses. The characteristic lattice configurations are shown in the inset. The schematics of microscopic mechanisms of MgO electronic excitations and melting processes under (B) LW laser pulses and (C) SW laser pulses.

Downloaded from https://spj.science.org at Institute of Physics, Cas on March 07, 2025

(RMSD), $\langle u^2(t)\rangle^{1/2}$, reaches the critical value of $R_c = 0.32$ Å (defined as melting line here, roughly 15% of the Mg–O bond length). On Born–Oppenheimer PESs, the RMSD is well below R_c with temperature below thermal melting point of ~3,200 K. Figure 2A and B shows the evolutions of RMSD under irradiations of SW and LW laser pulses, respectively. For the SW laser pulses, the maximums of RMSD are all located below the melting line for laser intensity I ranging from 3 to 47 TW/cm^2, reflecting the finite lattice heating and stability of lattice structure. In sharp contrast, the RMSD surpasses the melting threshold R_c within 100 fs for the LW pulses with $I \geq 15$ TW/cm^2. Then, the RMSD fluctuates with a large average value for I ranging from 15 to 24 TW/cm^2 and diverges for $I \geq 24$ TW/cm^2. The corresponding snapshots of lattice structures are shown in Fig. S1A. The divergence of RMSD and the convergence of radial distribution functions (Fig. S1B) unambiguously demonstrate the photoinduced ultrafast melting of MgO for $I \geq 24$ TW/cm^2. For I from 15 to 24 TW/cm^2, the large RMSD corresponds to the disordering and amorphization of lattice structure, and the amplitudes reflect the extent of configuration amorphization. Then, the subsequent relaxation leads to the restoration of PESs and the partial recovery of lattice structures, and the stronger electronic excitations require more time to relax. At this range, the atomic temperatures are still less than thermal melting point (Fig. S2). This is also regarded as "melting" in time-resolved x-ray diffraction experiments [46], where the structural disorders lead to the rapid decreases of diffraction intensities. Therefore, the LW laser can efficiently induce the lattice melting of MgO crystal.

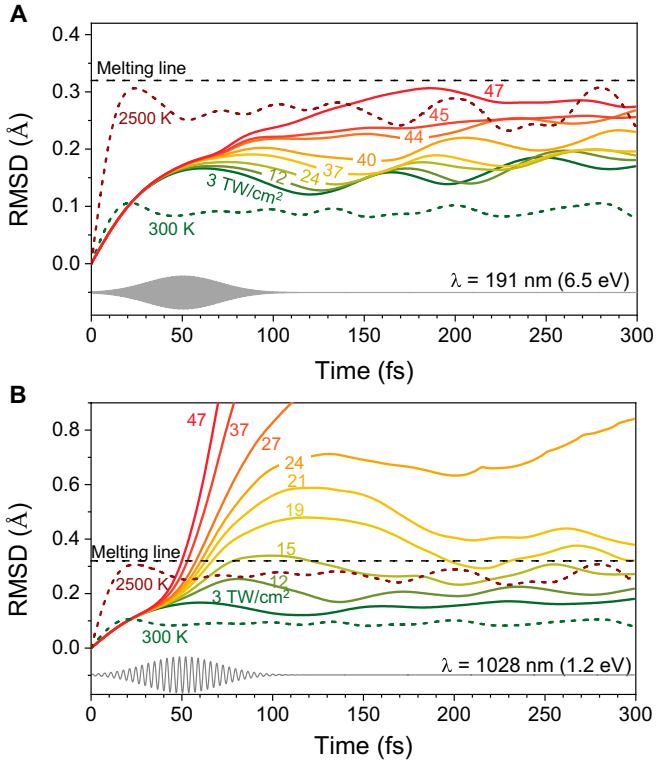

Fig. 2. The structural evolution of MgO under laser irradiations. The RMSD evolutions at different laser intensities for (A) SW 191-nm laser pulses and (B) LW 1,028-nm laser pulses. Melting line correspond to the Lindemann stability limit of $R_c = 0.32$ Å. The gray line in the inset shows the shape of laser pulse. The RMSD evolutions at Born–Oppenheimer PESs are shown in dotted lines.

The distinct lattice dynamics of MgO result from different photoexcitation strengths and photocarrier evolutions. The laser irradiations excite the valence electron to the conduction band, and the photocarriers then undergo the relaxation processes. Figure 3A shows the representative evolutions of photoexcited electrons for the LW and SW laser pulses. The electronic excitations are strongest at t_1 ~ 51 fs when the laser intensity reaches its maximum for LW laser pulses, and then decrease until the end of laser pulse (t_2 ~ 100 fs). Figure 3B exhibits the photoexcited electrons with the intensities of SW and LW laser pulses at t_1 and t_2, respectively. With the critical laser intensity I_{th} ~ 15 TW/cm^2, the LW laser pulses excite a large fraction (approximately 11%) of the valence electrons to the conduction band at t_1, and the excitation fraction is close to the reported threshold (~10%) in ultrafast nonthermal melting experiments [14]. However, the numbers of photoexcited electrons are relatively small for the SW laser pulses.

In general, the photoionization process is initiated by the resonant absorption under above-gap laser irradiations. However, the intense laser irradiations here can lead to strong nonlinear processes, e.g., multiphoton absorption and tunnel ionization. The significant roles of nonlinear processes were also observed in photoexcited germanium [27] under intense laser irradiations of 8 TW/cm^2. The specific nonlinear transition pathways are determined according to Keldysh theory [47,48], and the Keldysh parameter γ is defined as $\frac{\omega}{eE_0}\sqrt{m\Delta_g}$, where ω is the laser frequency, m is the reduced mass of the electron-hole pair, and Δ_g is the band gap of the material. The SW laser pulses have the Keldysh parameter $\gamma > 1$, and the multiphoton processes dominate the nonlinear transition pathway. The photoionization process includes the nonlinear 2-photon absorption besides the linear single-photon absorption. The single-photon absorption is the dominant ionization process under weak SW laser pulses (Fig. S3A). With the increase of SW laser intensity, the single-photon absorption is saturated due to the finite local electronic density of states (Fig. S3B and C), and the 2-photon absorption gradually contributes to the electronic excitation. As a result, the total excited electron n_e shows a linear relationship with SW laser intensity (Fig. 3C). On the other hand, the Keldysh parameter γ is less than 0.21 (labeled by the black arrow in Fig. 3D) for LW laser pulses with intensity above melting threshold $I_{th} = 15$ TW/cm^2, and thus, the nonlinear transition pathway is accounted by tunnel ionization (Fig. S3F), and n_e scales as $I^{0.5}$. However, the finite electronic density of states also restricts the 2-photon processes under weak LW laser irradiations (Fig. S3D), and the joint contributions of 2-photon processes and tunnel ionizations lead the linear relationship for weaker LW laser pulses (Fig. S4). The single-photon process is absent for LW laser due to the small photon energy. The relationship between electronic excitation and LW intensity in Fig. 3D is well consistent with that of photoexcited fused silica [49]. The tunnelling electrons can be broadly distributed on the conduction bands for LW pulses, while the discrete electronic distributions show up in single-photon and 2-photon absorption depending on the specific local electronic density of states and the rate of photocarrier relaxation. As a result, the LW laser leads to stronger electronic excitations than SW laser owing to a large number of electronic transition pathways. It is noted that the underestimation of band gap leads to the overestimation of transition intensity from multiphoton absorption to tunnel ionization by a factor of ~1.7 and overestimates the tunnel efficiency for long wavelength laser pulses.

Downloaded from https://spj.science.org at Institute of Physics, Cas on March 07, 2025

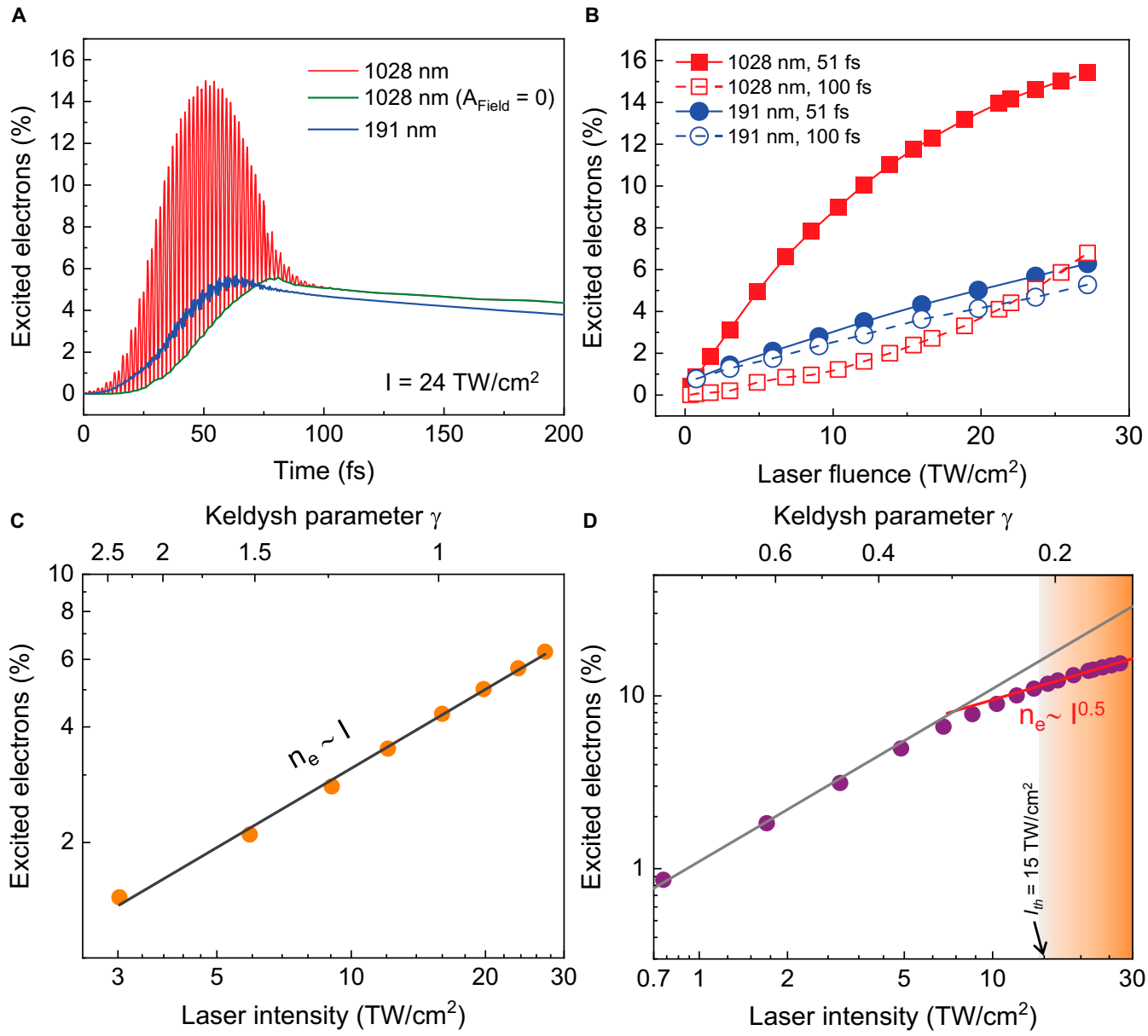

Fig. 3. The temporal evolutions of electronic excitation and the photoionization mechanisms. (A) Temporal evolutions of photoexcited electrons under the laser irradiations with intensity of 24 TW/cm^2. (B) Comparison of the photoexcited electrons under LW (squares) and SW (circles) laser pulses at 51 fs (solid symbols) and 100 fs (hollow symbols). The respective photoionization mechanisms for (C) SW and (D) LW laser pulses. Under the LW laser pulses, the system melts in the shaded area corresponding to Keldysh parameter $\gamma < 0.21$.

After the laser pulses, the remaining electronic excitations have only less than 5% valence electrons at t_2 for LW laser pulses. The fast electron-hole recombination accounts for the decrease of electronic excitations and leads to energy transfer to atomistic systems, and thus, the atomistic temperatures rapidly increase during the LW laser pulses (Fig. S2). The electron-hole recombination can be determined from the differences between the numbers of excited electrons at t_1 and t_2. The carrier recombination is relatively weak for the SW laser pulses. The LW laser irradiations trigger the effective electronic excitation and fast electronic relaxation in MgO during the laser pulses. We note that the avalanche effects are not included in the simulations due to finite simulation cell, and the avalanche effects play a key role via impact ionization processes for picosecond-long laser pulses.

The distinct carrier evolutions and energy transfer efficiencies of 2 laser pulses are attributed to the different carrier–carrier and carrier–phonon scattering processes, which also results in the unique distributions on time-dependent electronic density of states. At the initial stage, the tunnelling electrons exhibit the exponential distribution with the energy differences for LW laser pulses (Fig. S5). The continuous carrier distribution and Bloch oscillation of photocarriers [50] accelerate the carrier–carrier scattering processes, which enables the broad redistributions of photocarriers in the electron energy bands and promotes the fast equilibrium process within electronic subsystems. However, the discrete single-photon and 2-photon absorptions lead to the local occupations of photocarriers for SW laser pulses, which restricts the carrier–carrier scattering processes as shown in Fig. 4A. Further, the carrier–phonon scattering also

Downloaded from https://spj.science.org at Institute of Physics, Cas on March 07, 2025

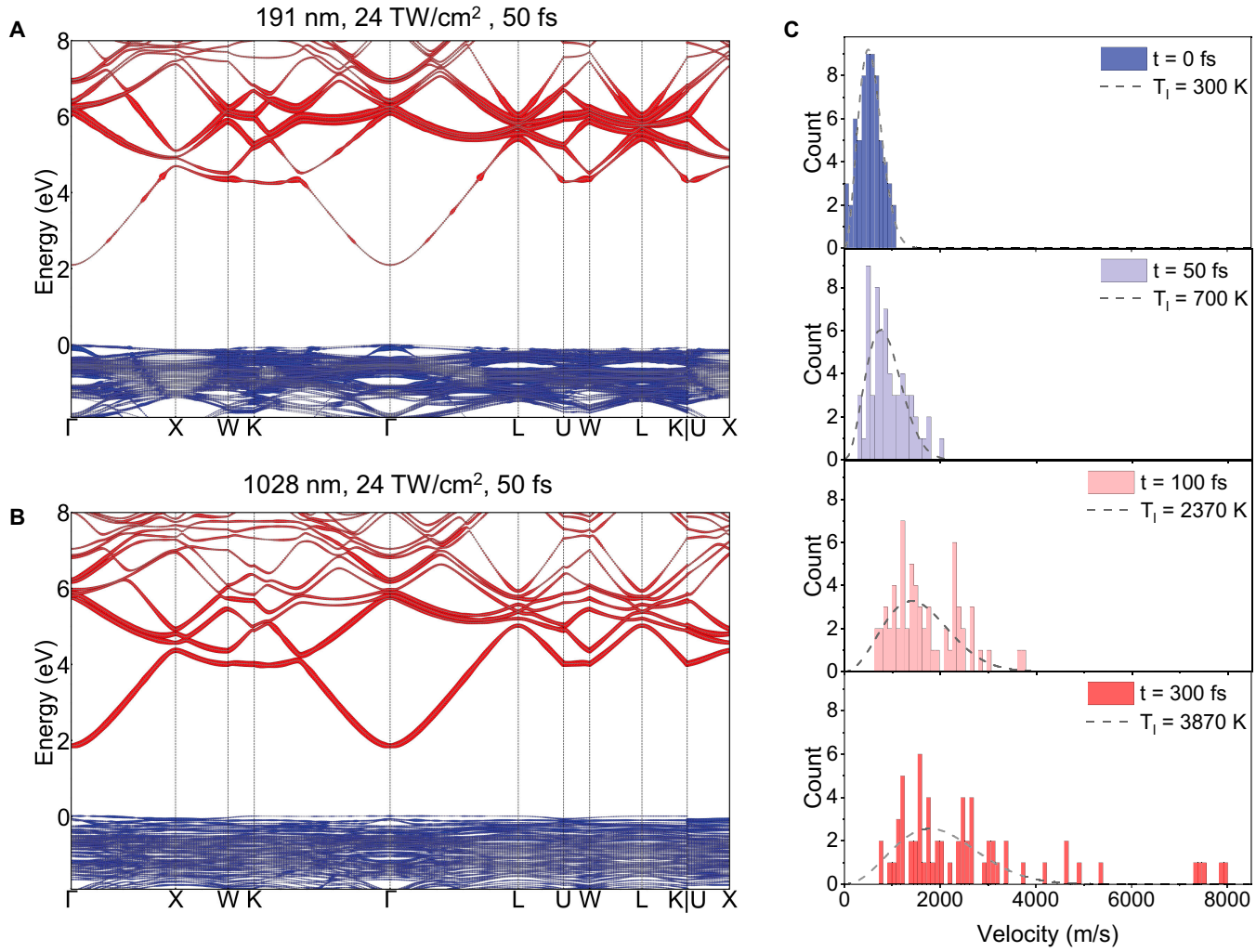

Fig. 4. The nonequilibrium carrier occupation and atom velocity distribution upon photoexcitation. The momentum- and energy-resolved photocarrier occupations under (A) SW and (B) LW laser pulses. The blue and red colors denote the occupation of photoexcited holes and electrons, respectively. The thickness of energy bands is scaled to represent the excitation strengths. (C) Temporal evolution of atom velocity distributions for LW laser pulse with intensity of 24 TW/cm^2. The gray lines represent the Maxwell distribution at different lattice temperatures.

shows the different rates for both laser pulses. We choose the electron–phonon coupling (EPC) matrix diagonal elements g_{ii} of lowest unoccupied band at Γ point and the transverse optical (TO) phonon reflecting Mg–O bond length oscillation as an example (Fig. S6). The g_{ii} value is 256 meV/Å under LW laser irradiation, which is 4 times larger than that of 57 meV/Å under SW laser irradiation with the same laser intensity. The strong EPC under LW laser irradiation enables the efficient energy transfer from carriers to the lattices during laser pulses (Fig. S2) and contributes to the fast electron redistribution as well. As a result, the tunnel ionization and fast relaxation lead to a broad distribution of photocarriers for LW laser pulses (Fig. 4B), while the photocarrier distribution remains discrete for SW laser pulses due to selective electronic transition and weak scattering processes (Fig. 4A). The faster energy transfer accounts well for the enhanced heat accumulations under LW laser pulses in Fig. 1A.

After the 100-fs-long photoexcitation and relaxation, the electronic subsystems relax into quasi-equilibrium states for LW laser pulses as shown in Fig. S7, and the instantaneous electron occupation exhibits the quasi-Fermi–Dirac (FD) distribution with a high electronic temperature [51] of ~25,000 K for LW with I = 24 TW/cm^2. The strong electronic excitations lead to phonon softening and the emergence of imaginary phonons in reciprocal space (Fig. S8), demonstrating the changes of PESs of lattice configurations. From t = 100 fs to t = 300 fs, the absorbed laser energy is continuously transferred from electrons to the lattice by EPC processes, and thus, the electronic subsystems gradually cool down (Fig. S7). The lattice receives the deposited energy and even reaches the thermal melting temperature within 300 fs for LW laser intensity above 21 TW/cm^2 (Fig. S2). Furthermore, the atomic velocity distributions deviate from the equilibrium Maxwell distribution in Fig. 4C, which demonstrates the non-equilibrium atomistic state and selective phonon excitations. As a result, the photoinduced ultrafast melting takes place at the femtosecond timescale (~100 fs) in a homogeneous manner owing to the changes of PESs and heating of atomic subsystems. This is in sharp contrast with the nucleation-growth manner at picosecond timescales (>10 ps) in classical nucleation theory. We note that the photoinduced ultrafast melting results in the final melting of crystal lattices when the energy absorbed

Downloaded from https://spj.science.org at Institute of Physics, Cas on March 07, 2025

surpasses that for thermal melting; otherwise, the amorphous structure will recrystallize after picosecond-long relaxation [52]. The photoinduced ultrafast melting features the nonequilibrium electronic and atomic states, ultrafast timescales, and homogeneous nucleation.

Discussion

Besides MgO, we also perform simulations for other ceramic materials such as aluminum nitride (AlN), which shows similar melting processes under the SW and LW laser pulse irradiations (Fig. S9). Figure S10 shows that the fluence thresholds for melting or damage decrease with the decrease of photon energies for a variety of wide-gap materials, and various laser wavelengths are employed. The decrease of photon energy leads to the decrease of Keldysh parameters and the enhancements of tunnel ionization processes, which accelerates the electronic excitations and ultrafast melting dynamics. The above evidences imply a universal mechanism of photoinduced ultrafast melting for wide-gap materials.

A detailed characterization of MgO evolution is obtained on a wide range of pressure–temperature conditions (especially at moderate pressure regime) as shown in Fig. 5. Three phases of MgO are present in its phase diagram: the B1 phase [30,53], the liquid phase, and a high-pressure phase with CsCl-type (B2) structure [54]. A nominal phase boundary between B1 and liquid phase can be obtained under laser irradiations with intensity exceeding the damage threshold. The predicted melting line lies below that for thermal equilibrium phase transition by Soubiran and Militzer [29], corresponding to the softening of PES via electronic excitations [55]. Coincidently, the nonequilibrium melting line has the same tendency with the preheated Hugoniot data (at $T_0 = 1{,}850$ K) by Fat'yanov et al. [56].

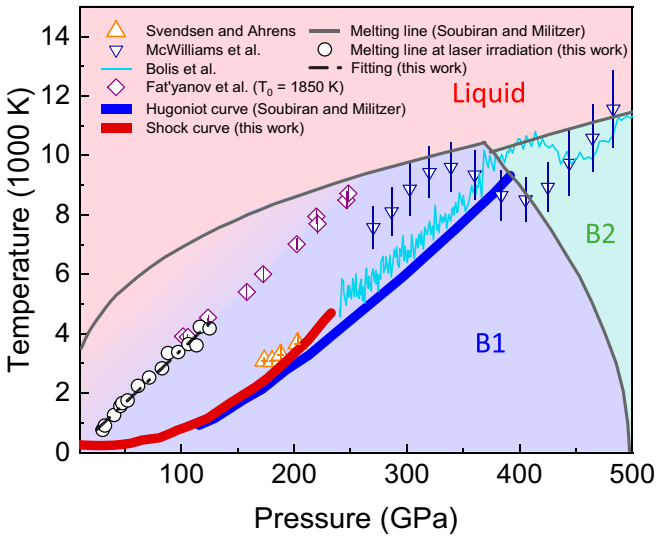

Fig. 5. Phase diagram of MgO including shock wave curves and melting lines under laser irradiation. The gray lines (Soubiran and Militzer [29]) denote the phase boundary between the B1 (NaCl-type structure, purple), liquid (pink), and B2 (CsCl-type structure, green) phases. The thick lines correspond to the shock curve calculated here (red) and the Hugoniot curve from literature (blue) (Soubiran and Militzer [29]) for the B1 phase. The experimental results of single shocks (Svendsen and Ahrens [30]) and decaying shocks (McWilliams et al. [28]; Bolis et al. [31]) are also included. The melting data under laser irradiation (black circle) can be fitted linearly (black dashed dotted line), which have the same tendency with the experimental Hugoniot curve (purple diamond square) measured after preheating (Fat'yanov et al. [56]).

Our advanced TDDFT-MD approach enables us to simulate the generations of shock waves and extend it to moderate pressure regimes ($P = 2$ GPa) (Fig. 5). The Hugoniot line at $P = 1$ to 100 GPa is of great significances for geoscience and planetary science, phase transitions of materials, and explosion engineering, as these processes usually take place at $P = 1$ to 100 GPa. However, the requirements of high accuracy and computational burdens restrict the study of Hugoniot line at this range in previous studies [29]. Here, the shock curve under the laser irradiations can be calculated by recording the temperature and pressure at the maximum amplitude of laser pulse (Fig. S11). The obtained smallest pressure is ~2 GPa at the Hugoniot line (Fig. S12). The predicted shock curve in B1 phase is close to the experimental single-shock data [30], and its extrapolation at large pressure regime is consistent with the decaying shock measurements [28,31], which demonstrates the reliability of our prediction method and the extension to moderate regimes. The inclusion of the nonequilibrium states makes the shock curve prediction more realistic, and the predicted shock curve exhibits better consistency than estimations from empirical Hugoniot curve [29].

Conclusion

In conclusion, the coupled electron–lattice dynamics of MgO under laser illuminations are investigated based on first-principles quantum-classical dynamics simulations. The lower intensity threshold of ultrafast melting under LW laser pulses is attributed to the strong-field-induced tunnel ionization process, and a large number of valence electrons are excited to the conduction bands leading to intense energy absorption. The instantaneous changes of PES and fast energy transfer from electrons to the lattice via strong EPC lead to ultrafast lattice response and subsequent melting of crystal structure. This work not only offers new insights into the nonequilibrium mechanisms of laser-induced phase transition in ceramics but also demonstrates the possibility of manipulating phase transition at ambient conditions via laser irradiations. Our study is of great significance to ultrafast physics, extreme condition physics, and advanced material manufacturing.

Acknowledgments

Funding: We acknowledge partial financial support from National Key Research and Development Program of China (no. 2021YFA1400200), National Natural Science Foundation of China (nos. 12025407, 11934003, and 12204513), and "Strategic Priority Research Program (B)" of Chinese Academy of Sciences (grant nos. XDB330301 and YSBR047).
Author contributions: H.Z., J.X., and S.M. designed the research. H.Z. and S.H. performed the research. M.G., X.L., and D.C. contributed computational and analytical tools. H.Z. and J.X. analyzed the data. H.Z., J.X., and S.M. wrote the paper.
Competing interests: The authors declare that they have no competing interests.

Data Availability

The data that support the findings of this study are available from the corresponding author upon reasonable request.

Supplementary Materials

Figs. S1 to S12

Downloaded from https://spj.science.org at Institute of Physics, Cas on March 07, 2025

References

1. Sundaram SK, Mazur E. Inducing and probing non-thermal transitions in semiconductors using femtosecond laser pulses. *Nat Mater*. 2002;1(4):217–224.
2. Siders CW, Cavalleri A, Sokolowski-Tinten K, Tóth C, Guo T, Kammler M, Horn von Hoegen M, Wilson KR, von der Linde D, Barty CP. Detection of nonthermal melting by ultrafast X-ray diffraction. *Science*. 1999;286(5443):1340–1342.
3. Zhang P, Chung T-F, Li Q, Wang S, Wang Q, Huey WLB, Yang S, Goldberger JE, Yao J, Zhang X. All-optical switching of magnetization in atomically thin CrI_3. *Nat Mater*. 2022;21(12):1373–1378.
4. Budden M, Gebert T, Buzzi M, Jotzu G, Wang E, Matsuyama T, Meier G, Laplace Y, Pontiroli D, Riccò M, et al. Evidence for metastable photo-induced superconductivity in K_3C_{60}. *Nat Phys*. 2021;17(5):611–618.
5. Recoules V, Clérouin J, Zérah G, Anglade PM, Mazevet S. Effect of intense laser irradiation on the lattice stability of semiconductors and metals. *Phys Rev Lett*. 2006;96(5): Article 055503.
6. Chen N-K, Li X-B, Bang J, Wang X-P, Han D, West D, Zhang S, Sun H-B. Directional forces by momentumless excitation and order-to-order transition in Peierls-distorted solids: The case of GeTe. *Phys Rev Lett*. 2018;120(18):Article 185701.
7. Rousse A, Rischel C, Fourmaux S, Uschmann I, Sebban S, Grillon G, Balcou P, Förster E, Geindre JP, Audebert P, et al. Non-thermal melting in semiconductors measured at femtosecond resolution. *Nature*. 2001;410(6824):65–68.
8. Li X, Qiu T, Zhang J, Baldini E, Lu J, Rappe AM, Nelson KA. Terahertz field-induced ferroelectricity in quantum paraelectric $SrTiO_3$. *Science*. 2019;364(6445):1079–1082.
9. Guan MX, Liu XB, Chen DQ, Li XY, Qi YP, Yang Q, You PW, Meng S. Optical control of multistage phase transition via phonon coupling in $MoTe_2$. *Phys Rev Lett*. 2022;128(1): Article 015702.
10. Zhang J, Lian C, Guan M, Ma W, Fu H, Guo H, Meng S. Photoexcitation induced quantum dynamics of charge density wave and emergence of a collective mode in 1*T*-TaS_2. *Nano Lett*. 2019;19(9):6027–6034.
11. Harb M, Ernstorfer R, Hebeisen CT, Sciaini G, Peng W, Dartigalongue T, Eriksson MA, Lagally MG, Kruglik SG, Miller RJD. Electronically driven structure changes of Si captured by femtosecond electron diffraction. *Phys Rev Lett*. 2008;100(15):Article 155504.
12. Lian C, Zhang SB, Meng S. Ab initio evidence for nonthermal characteristics in ultrafast laser melting. *Phys Rev B*. 2016;94(18):Article 184310.
13. Liu WH, Luo JW, Li SS, Wang LW. The seeds and homogeneous nucleation of photoinduced nonthermal melting in semiconductors due to self-amplified local dynamic instability. *Sci Adv*. 2022;8(27):eabn4430.
14. Sciaini G, Harb M, Kruglik SG, Payer T, Hebeisen CT, zu Heringdorf FJ, Yamaguchi M, Horn von Hoegen M, Ernstorfer R, Miller RJD. Electronic acceleration of atomic motions and disordering in bismuth. *Nature*. 2009;458(7234):56–59.
15. Sokolowski-Tinten K, Blome C, Dietrich C, Tarasevitch A, Horn von Hoegen M, von der Linde D, Cavalleri A, Squier J, Kammler M. Femtosecond X-ray measurement of ultrafast melting and large acoustic transients. *Phys Rev Lett*. 2001;87(22):Article 225701.
16. Mo M, Murphy S, Chen Z, Fossati P, Li R, Wang Y, Wang X, Glenzer S. Visualization of ultrafast melting initiated from radiation-driven defects in solids. *Sci Adv*. 2019;5(5):eaaw0392.
17. Siwick BJ, Dwyer JR, Jordan RE, Miller RJD. An atomic-level view of melting using femtosecond electron diffraction. *Science*. 2003;302(5649):1382–1385.
18. Ernstorfer R, Harb M, Hebeisen CT, Sciaini G, Dartigalongue T, Miller RJD. The formation of warm dense matter: Experimental evidence for electronic bond hardening in gold. *Science*. 2009;323(5917):1033–1037.
19. Jourdain N, Lecherbourg L, Recoules V, Renaudin P, Dorchies F. Ultrafast thermal melting in nonequilibrium warm dense copper. *Phys Rev Lett*. 2021;126(6):Article 065001.
20. Rethfeld B, Ivanov DS, Garcia ME, Anisimov SI. Modelling ultrafast laser ablation. *J Phys D Appl Phys*. 2017;50: Article 193001.
21. Xiong S, Wang R, Tao H. Ultrafast laser micromachining the ultra-low expansion glass-ceramic: Optimization of processing parameters and physical mechanism. *J Eur Ceram Soc*. 2021;41(12):5990–5999.
22. Itoh K, Watanabe W, Nolte S, Schaffer CB. Ultrafast processes for bulk modification of transparent materials. *MRS Bull*. 2006;31(8):620–625.
23. Penilla EH, Devia-Cruz LF, Wieg AT, Martinez-Torres P, Cuando-Espitia N, Sellappan P, Kodera Y, Aguilar G, Garay JE. Ultrafast laser welding of ceramics. *Science*. 2019;365(6455):803–808.
24. Vogel A, Noack J, Hüttman G, Paltauf G. Mechanisms of femtosecond laser nanosurgery of cells and tissues. *Appl Phys B*. 2005;81(8):1015–1047.
25. Gattass RR, Mazur E. Femtosecond laser micromachining in transparent materials. *Nat Photonics*. 2008;2(4):219–225.
26. Xu J, Chen D, Meng S. Probing laser-induced plasma generation in liquid water. *J Am Chem Soc*. 2021;143(27):10382–10388.
27. Inzani G, Adamska L, Eskandari-asl A, Di Palo N, Dolso GL, Moio B, D'Onofrio LJ, Lamperti A, Molle A, Borrego-Varillas R, et al. Field-driven attosecond charge dynamics in germanium. *Nat Photonics*. 2023;17(12):1059–1065.
28. McWilliams RS, Spaulding DK, Eggert JH, Celliers PM, Hicks DG, Smith RF, Collins GW, Jeanloz R. Phase transformations and metallization of magnesium oxide at high pressure and temperature. *Science*. 2012;338(6112):1330–1333.
29. Soubiran F, Militzer B. Anharmonicity and phase diagram of magnesium oxide in the megabar regime. *Phys Rev Lett*. 2020;125(17):Article 175701.
30. Svendsen B, Ahrens TJ. Shock-induced temperatures of MgO. *Geophys J Int*. 1987;91(3):667–691.
31. Bolis RM, Morard G, Vinci T, Ravasio A, Bambrink E, Guarguaglini M, Koenig M, Musella R, Remus F, Bouchet J, et al. Decaying shock studies of phase transitions in MgO-SiO_2 systems: Implications for the super-Earths' interiors. *Geophys Res Lett*. 2016;43(18):9475–9483.
32. Bassman L, Krishnamoorthy A, Kumazoe H, Misawa M, Shimojo F, Kalia RK, Nakano A, Vashishta P. Electronic origin of optically-induced sub-picosecond lattice dynamics in $MoSe_2$ monolayer. *Nano Lett*. 2018;18(8):4653–4658.
33. Guan MX, Wang E, You PW, Sun JT, Meng S. Manipulating Weyl quasiparticles by orbital-selective photoexcitation in WTe_2. *Nat Commun*. 2021;12(1):1885.
34. Xu J, Chen D, Meng S. Decoupled ultrafast electronic and structural phase transitions in photoexcited monoclinic VO_2. *Sci Adv*. 2022;8(44):eadd2392.

Downloaded from https://spj.science.org at Institute of Physics, Cas on March 07, 2025

35. Meng S, Kaxiras E. Real-time, local basis-set implementation of time-dependent density functional theory for excited state dynamics simulations. *J Chem Phys*. 2008;129(5):054110.
36. Meng S, Ren J, Kaxiras E. Natural dyes adsorbed on TiO_2 nanowire for photovoltaic applications: Enhanced light absorption and ultrafast electron injection. *Nano Lett*. 2008;8(10):3266–3272.
37. Lian C, Guan M, Hu S, Zhang J, Meng S. Photoexcitation in solids: First-principles quantum simulations by real-time TDDFT. *Adv Theory Simul*. 2018;1(8):1800055.
38. Lian C, Hu SQ, Guan MX, Meng S. Momentum-resolved TDDFT algorithm in atomic basis for real time tracking of electronic excitation. *J Chem Phys*. 2018;149(15): Article 154104.
39. Ordejón P, Artacho E, Soler JM. Self-consistent order-N density-functional calculations for very large systems. *Phys Rev B*. 1996;53(16):R10441–R10444.
40. José MS, Emilio A, Julian DG, Alberto G, Javier J, Pablo O, Daniel S-P. The SIESTA method for *ab initio* order-N materials simulation. *J Phys Condens Matter*. 2002;14(11):2745.
41. Sánchez-Portal D, Ordejón P, Artacho E, Soler JM. Density-functional method for very large systems with LCAO basis sets. *Int J Quantum Chem*. 1997;65(5):453–461.
42. Marques MA, Maitra NT, Nogueira FM, Gross EK, Rubio A. *Fundamentals of time-dependent density functional theory*. Berlin, Heidelberg: Springer; 2012.
43. Troullier N, Martins JL. Efficient pseudopotentials for plane-wave calculations. II. Operators for fast iterative diagonalization. *Phys Rev B*. 1991;43(11):8861–8869.
44. Perdew JP, Burke K, Ernzerhof M. Generalized gradient approximation made simple. *Phys Rev Lett*. 1996;77(18): 3865–3868.
45. Zijlstra ES, Kalitsov A, Zier T, Garcia ME. Squeezed thermal phonons precurse nonthermal melting of silicon as a function of fluence. *Phys Rev X*. 2013;3(1):Article 011005.
46. Sokolowski-Tinten K, Blome C, Blums J, Cavalleri A, Dietrich C, Tarasevitch A, Uschmann I, Förster E, Kammler M, Horn-von-Hoegen M, et al. Femtosecond X-ray measurement of coherent lattice vibrations near the Lindemann stability limit. *Nature*. 2003;422(6929):287–289.
47. Keldysh LV. Ionization in the field of a strong electromagnetic wave. *Zh Eksperim Teor Fiz*. 1964;**47**.
48. Schultze M, Ramasesha K, Pemmaraju CD, Sato SA, Whitmore D, Gandman A, Prell JS, Borja LJ, Prendergast D, Yabana K, et al. Attosecond band-gap dynamics in silicon. *Science*. 2014;346(6215):1348–1352.
49. Chris BS, André B, Eric M. Laser-induced breakdown and damage in bulk transparent materials induced by tightly focused femtosecond laser pulses. *Meas Sci Technol*. 2001;12(11):1784.
50. Bloch F. Über die quantenmechanik der elektronen in kristallgittern. *Z Physik*. 1929;52(7-8):555–600.
51. Rohde G, Stange A, Müller A, Behrendt M, Oloff LP, Hanff K, Albert TJ, Hein P, Rossnagel K, Bauer M. Ultrafast formation of a Fermi-Dirac distributed electron gas. *Phys Rev Lett*. 2018;121(25):Article 256401.
52. Kirschner MS, Hannah DC, Diroll BT, Zhang X, Wagner MJ, Hayes D, Chang AY, Rowland CE, Lethiec CM, Schatz GC, et al. Transient melting and recrystallization of semiconductor nanocrystals under multiple electron–hole pair excitation. *Nano Lett*. 2017;17(9):5314–5320.
53. Duffy TS, Hemley RJ, Mao HK. Equation of state and shear strength at multimegabar pressures: Magnesium oxide to 227 GPa. *Phys Rev Lett*. 1995;74(8):1371–1374.
54. Coppari F, Smith RF, Eggert JH, Wang J, Rygg JR, Lazicki A, Hawreliak JA, Collins GW, Duffy TS. Experimental evidence for a phase transition in magnesium oxide at exoplanet pressures. *Nat Geosci*. 2013;6(11):926–929.
55. Murphy ST, Daraszewicz SL, Giret Y, Watkins M, Shluger AL, Tanimura K, Duffy DM. Dynamical simulations of an electronically induced solid-solid phase transformation in tungsten. *Phys Rev B*. 2015;92(13):Article 134110.
56. Fat'yanov OV, Asimow PD, Ahrens TJ. Thermodynamically complete equation of state of MgO from true radiative shock temperature measurements on samples preheated to 1850 K. *Phys Rev B*. 2018;97(2):Article 024106.

Downloaded from https://spj.science.org at Institute of Physics, Cas on March 07, 2025